JOURNAL OF GEOPHYSICAL RESEARCH, VOL. 106, NO. A10, PAGES 21,367–21,380, OCTOBER 1, 2001

Satellite limb tomography applied to airglow of the 630 nm emission

S. Frey, S. B. Mende, and H. U. Frey

Space Sciences Laboratory, University of California, Berkeley, California

Abstract. Airglow intensity variations in the 90 km altitude range are generally interpreted as the optical signature of gravity waves propagating through the airglow layer. In contrast, modulations of the 630 nm emission in the F region are subject to atmospheric wave propagation and ionospheric electrodynamics, which makes it difficult to determine the dominating process. Spacecraft-based imaging of the 630 nm airglow could produce global data of airglow modulations greatly needed for the understanding of thermospheric dynamics. Observations of the thick 630 nm airglow layer between 200 and 300 km altitude are used to demonstrate the ability to tomographically retrieve the modulated volume emission rates from limb observations from a spacecraft. An algebraic reconstruction technique is used to obtain vertical and horizontal distributions with average errors of 20%. Its effectiveness is demonstrated by simulations with numerical data. Forward limb observations in the 630 nm range strongly reduce the angular range and limit the measurement scale to 300 km. These results are obtained without any assumptions about the original distribution other than nonnegativity. The overall computational effort would allow the analysis of a large number of observations as provided by global survey experiments.

1. Introduction

For many years, gravity waves have been studied as a key element in the spatial and temporal variations above the troposphere. They arise from localized disturbances within the troposphere such as thunderstorms, deep convection regions, front systems in the lower atmosphere, and orographic forcing due to wind flow over mountains [*Hines,* 1967; *Hirota,* 1984; *Fritts and Luo,* 1992; *Bergman and Salby,* 1994; *Allen and Vincent,* 1995; *Alexander,* 1998; *Dewan et al.,* 1998]. While propagating upward, gravity waves carry a significant amount of energy and momentum, and they cause neutral wind perturbations. In the mesosphere and lower thermosphere, gravity waves have a dramatic impact on the thermal structure and hence the circulation [*Fritts and Vincent,* 1987; *McIntyre,* 1989; *Tarasick and Shepherd,* 1992; *Luo et al.,* 1995; *Swenson and Gardner,* 1998; *Swenson and Liu,* 1998]. In the ionosphere, depending on day or night conditions, neutral wind perturbations interact with plasma motion along magnetic field lines or with vertical motion of the ionosphere resulting in horizontally propagating height disturbances [*Beach et al.,* 1997; *Miller et al.,* 1997; *Singh et al.,* 1997].

Paper number 2001JA900024.
0148-0227/01/2001900024$09.00

Intensity fluctuations in the airglow emissions of the upper atmosphere are optical signatures of the gravity wave dynamics. Early reports of nonauroral brightness on a night sky go back to the end of the eighteenth century [*Chamberlain,* 1995]. With the support of rockets and satellites, as well as the development of highly sensitive remote sensing systems (optical, radar, and lidar), detailed investigations of the several emission layers have revealed the association of irregularities in the airglow pattern with the passage of internal gravity waves [*Taylor,* 1997; *Coble et al.,* 1998; *Garcia et al.,* 1997; *Gardner and Taylor,* 1998; *Swenson and Gardner,* 1998; *Swenson and Liu,* 1998]. According to their wide spectrum of wave parameters, gravity waves are currently distinguished as small-scale waves with horizontal wavelengths between a few and tens of kilometers and as large-scale waves with horizontal wavelengths above 1000 km. Intense investigation of small-scale waves has improved knowledge of the chemiluminescent response of the several airglow layers as well as the relationship between wave parameters [*Frederick,* 1979; *Armstrong,* 1982; *Taylor et al.,* 1997; *Frey et al.,* 2000; *Swenson et al.,* 2000].

The sampled data about large-scale waves in the ionosphere/thermosphere and the quantitative characterization of the global pattern of the upper atmospheric dynamics where the processes become more complex are much more limited [*Gardner and Taylor,* 1998]. Here ionospheric plasma parameters are controlled by solar

activity, geomagnetic disturbances, and superposition of external electric fields. Whether the intensity enhancements of the 630 nm emission are caused by upward propagating gravity waves acting directly on the F region or by some electrodynamic coupling processes still needs to be investigated. Two reported examples of 630 nm volume emission rates deduced from space-born as well as ground-based measurements document the manifoldness. A time series of events observed by the Wind Imaging Interferometer WINDII [*Shepherd et al.*, 1993] on UARS is interpreted in correlation with a geomagnetic substorm. Ground-based observations from the Arecibo observatory, with the support of electron density data from an ionosonde, are associated with F region gravity waves [*Mendillo et al.*, 1997]. Though different in the size of the disturbances, both experimental data indicate that the 630 nm layer is rather thick, and they support the theory of vertical variations of the emission heights in the F region.

The key parameter needed to fully understand the complexity and for the development of large-scale models can only be provided by space-born observations [*Mende et al.*, 1998]. In addition to the global survey, satellite-based forward limb observations of the airglow emission from consecutive positions along the satellite orbit enable the use of tomographic techniques, which invert the measured surface brightness into an estimate of the volume emission rate and hence provide information about both the vertical and the horizontal dimensions.

Many tomographic approaches are based on Fourier transformations of equally spaced observations. The quality of the final reconstruction is strongly related to the angular coverage. The best known application is the medical diagnosis in which an instrument is rotated around the patient [*Budinger and Gullberg*, 1974].

In contrast, ground-based and space-born measurements, and, in particular, limb observations from a moving spacecraft, cover only a limited angular range. The temporal variability in the source distribution becomes a constraining factor as it may be of the order of the observation interval. Furthermore, the observations are made through a medium that may contaminate the data.

Various non-transform-based tomographic techniques have been developed to address these constraints. Among them are applications to recover the spatial distribution of airglow and auroral emissions and the electron density distribution in the ionosphere. They use different mathematical methods and various ways to incorporate models and noise distribution and to account for contamination [*Aso et al.*, 1990; *Vallance Jones et al.*, 1991; *Raymund et al.*, 1993; *Doe et al.*, 1997; *Bernhardt et al.*, 1998; *Gustavsson*, 1998; *Semeter et al.*, 1999].

The use of satellite limb observations of the OI 557.7 nm emission in the F region, where the field of view is horizontally directed along the emission layer, initiated the application of tomography in atmospheric physics [*Thomas and Donahue*, 1972]. Since then, a variety of methods have been applied to the earthward directed observations despite constraints to exclude brightness modulations caused by the Earth albedo. Reliable altitude profiles for discrete auroral features at several wavelengths as well as for the 630 nm emission rates were obtained from the one-dimensional (1-D) data of the Visible Airglow Experiment (VAE). The spinning mode of the satellite significantly improved the angular coverage, and a transform-based algorithm could be applied [*Fesen and Hays*, 1982; *Solomon et al.*, 1984, 1985]. The VAE data greatly contributed to the current understanding of the chemistry and dynamics of the upper thermosphere [*Fesen and Abreu*, 1987; *Solomon et al.*, 1988; *Burrage et al.*, 1991].

The possibility of recovering airglow structures from limb emission profiles was only demonstrated with spatially simulated low-contrast small-scale (200 - 800 km) emission features in the 80-100 km altitude region by using an iterative probability method [*McDade and Llewllyn*, 1993]. Very recent developments use emissions in the EUV range [*Kamalabadi et al.*, 1999] and employ statistical inversion algorithms.

In this paper we examine the effectiveness of satellite limb tomography in the measurement of spatial variation of the 630 nm airglow. An example of topside limb 630 nm data is provided by WINDII (G. Shepherd, private communication, 2000), which shows the inherent structure combined with global coverage. The effectiveness of tomographic limb observations is examined with a model of periodic patterns of 630 nm emission. We also apply our technique to airglow emission rates computed from ground-based measured electron densities [*Mendillo et al.*, 1997]. In accordance with satellite-based simulations we constrain the viewing geometry to eliminate the scatter from the Earth albedo and other contaminations. The selected orbit height conforms with the need to address current goals in the study of the influence of gravity waves on the global upper atmospheric dynamics. The large orbit height, the small limb field of view, and the irregular data within a relatively thick layer not only comprise a very challenging tomographic constellation but require a computational, fast algorithm that provides sufficient resolution despite large distances. We will show that the tomographic technique permits the recovery of airglow structures relevant to ground-based measurements [*Mendillo et al.*, 1997].

The chosen algebraic tomographic technique is based on results in 3-D stereographic auroral tomography with ground-based data and studies for magnetospheric applications [*Frey et al.*, 1996, 1998b]. From simulated low-contrast emission rates in the mesopause region [*McDade and Llewellyn*, 1993] and the inversion of auroral and airglow 630 nm emissions from the VAE data of a spinning satellite [*Solomon et al.*, 1984], results were obtained that have established atmospheric satel-

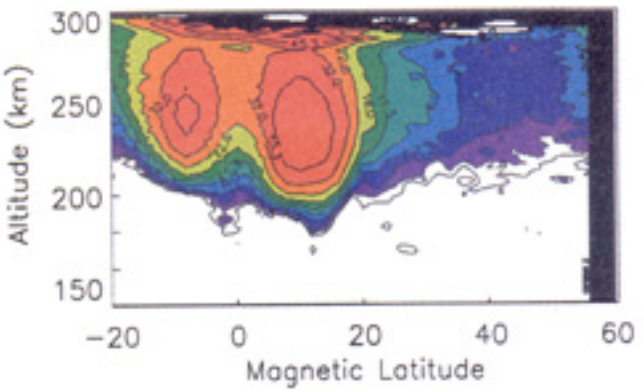

Plate 1. The 630 nm airglow emission rate (photons $cm^{-3}s^{-1}$) observed by WINDII on UARS at 248.1 longitude: UT=0860, LT=0120.

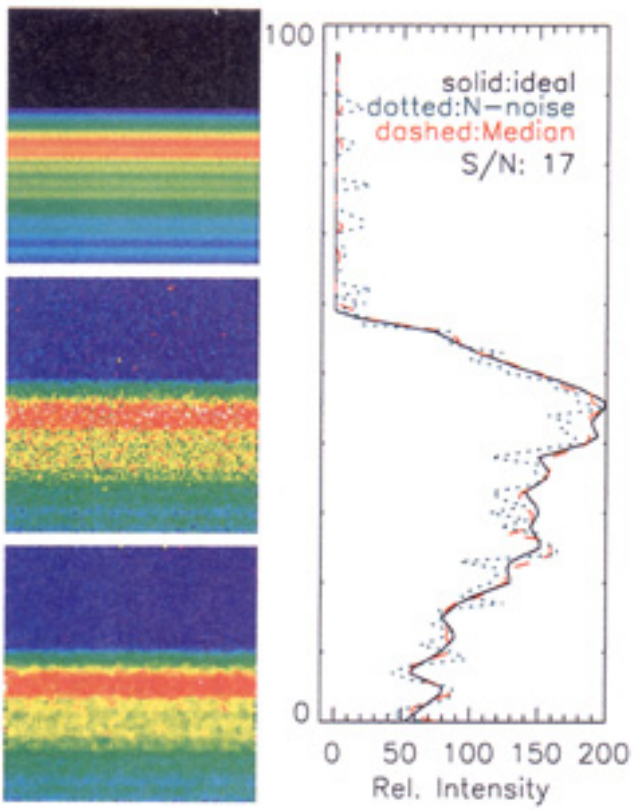

Plate 2. A single 2-D limb view comparing the (top left) ideal data, (middle left) data deteriorated by noise, and (bottom left) deteriorated data after a median filter was applied and (right column) a vertical line scan along the field of view.

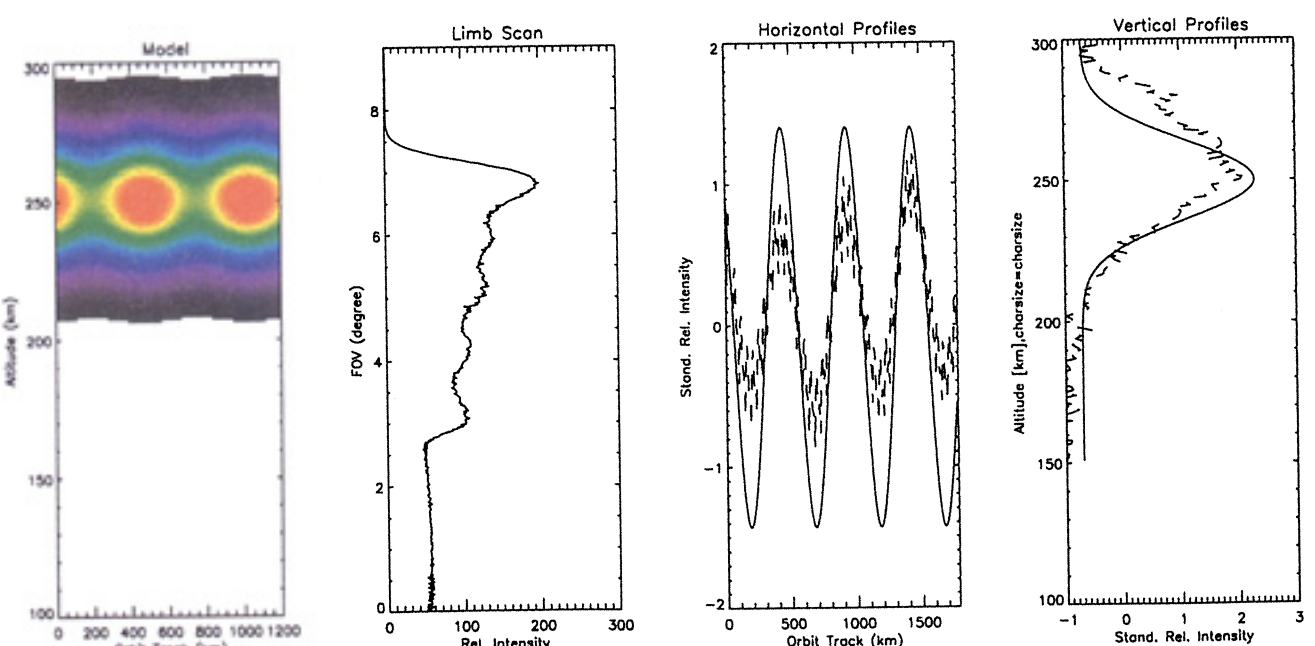

Plate 3. The angular view of the quasi-limb observations revealing both the horizontal and the vertical modulations of the reconstructed data: (left) a thin emission layer with a horizontal wavelength of 500 km, an (middle left) arbitrary limb scan, and (middle right) horizontal and (right) vertical profiles of the original (solid) and reconstructed (dashed) data.

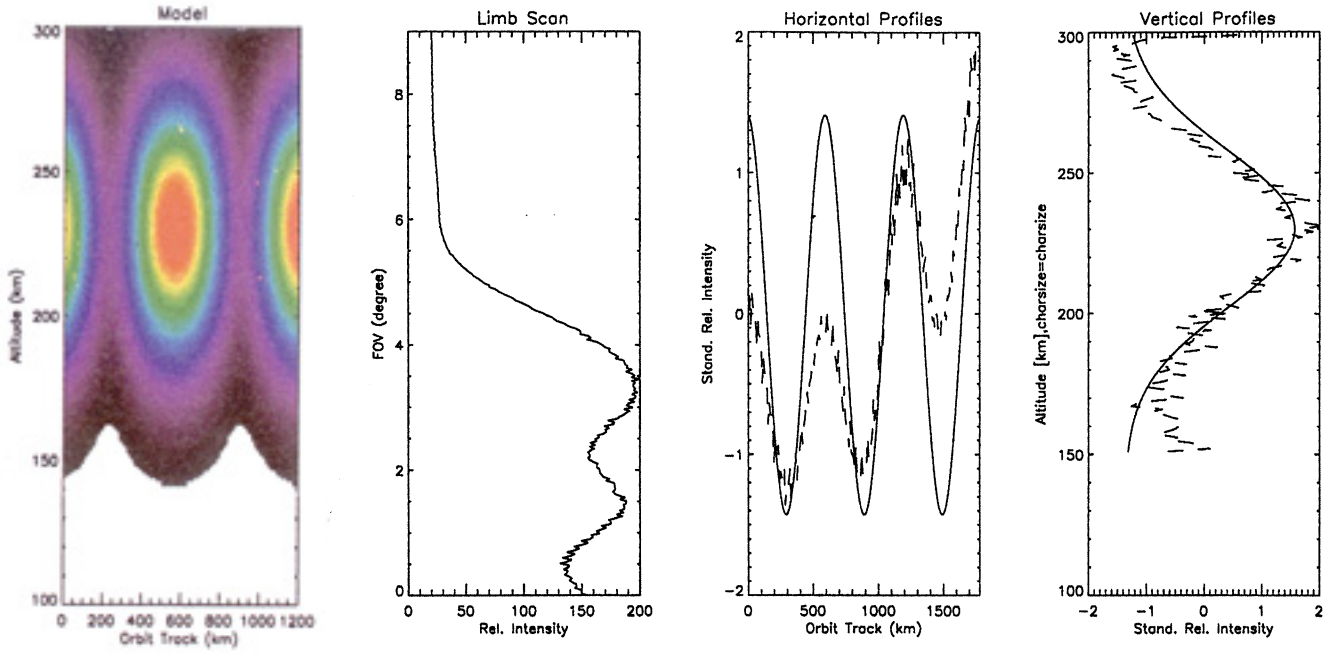

Plate 4. Similar to Plate 3 but showing the resolution of the thick 630 nm emission layer with a horizontal wavelength of 600 km reconstructed from limb observations.

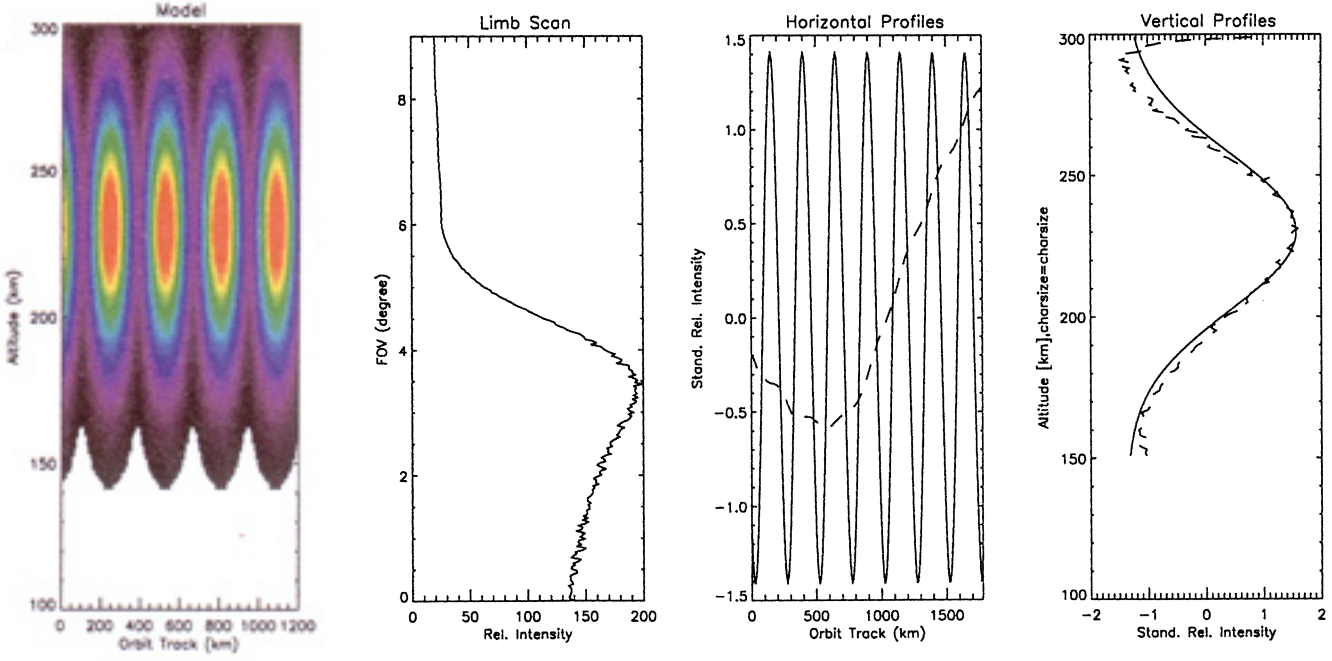

Plate 5. Similar to Plate 3 but showing the cutoff in the horizontal resolution, with the thick 630 nm emission layer and a horizontal wavelength of 250 km reconstructed from limb observations.

lite tomography. Now we would like to combine both approaches by reconstructing the thicker layer of the 630 nm emission with only the forward limb projections and a computational effort that allows the analysis of global coverage data.

The feasibility of the employed tomographic technique under the new conditions still needs verification. In that sense, applying satellite limb tomography to the F region dynamics is a new approach.

2. Tomographic Methods

Tomography summarizes techniques to solve the inverse problem to reconstruct an unknown n-dimensional source distribution from a set of n-1-dimensional remote measurements. In optical observations the projections $p_i(\theta, \phi)$ are determined by the integral of the volume emission along lines from the observer position at $\mathbf{r} = 0$ through the object:

$$p_i(\theta,\phi) = C \int_0^\infty f[\mathbf{r}(l)] \exp\left[-\int_{s=0}^{s=l} \mu(s) ds\right] dl, \quad (1)$$

with the source distribution $f(\mathbf{r})$ and an absorption term $\mu(s)$. In general, the unknown quantity is either the source distribution, the distribution of the absorbing matter, or both.

In the 2-D computerized discrete case the observation plane is divided into small pixels (x, y), with the value in each pixel representing the mean of the source distribution $f(x, y)$. The constant parameter C contains measurement parameters such as spectral sensitivity, solid angle for the observation, and filter and lens transmission. We approximate the absorption as constant and simplify (1) to

$$p_i(\theta) \approx C' \sum_{x,y} h_{xy}^{i\theta} f(x,y), \quad (2)$$

with $h_{xy}^{i\theta}$ describing the contribution of the pixel (x, y) to the region subtended by the ray for the projection i. The measurement geometry is based on diverging fan beams with angle γ, which requires projections in an angular region:

$$\theta_0 \le \theta < \theta_0 + 180^\circ + 2\gamma. \quad (3)$$

The goal of tomographic studies, in general, is to solve the set of linear equations (2). Various methods have been developed to find an estimate $\hat{f}$ of f based on Fourier transform, algebraic, and statistical methods [*Budinger und Gullberg,* 1974; *Natterer,* 1986; *Verhoeven,* 1993].

Most geophysical applications cannot provide the necessary angular coverage of observations (3), which leads to the so-called missing cone problem [*Hayner and Jenkins,* 1984]. A further characteristic of geophysical applications is that the objects are generally smooth with features of similar contrast. There are no sharp borders as in medical tomography bones. The lines of sight cut through inhomogeneous source distributions. In our study these disadvantages are amplified because of the constraint of a very small field of view and the large-scale structures in the 630 nm range. Eventually, our optical data are discrete, deteriorated by noise, and limited in number within the angular range. To recover the source distribution with sufficient accuracy, the use of a priori information about the object's smoothness, extent, or nonnegativity may compensate for the ill-conditioned data set.

With ill-conditioned data the direct inverse methods are of limited use. Statistical methods can provide the most satisfying results for data with isolated peaks and with incorporation of noise distribution [*Nygrén et al.,* 1996]. Inversion by singular value decomposition handles many problems associated with ill conditioning but is far too computationally intensive for the large dimensions encountered in satellite limb data sets. If the original distribution is known to be reasonably smooth, then a least squares (LS) method can be used [*Frey et al.,* 1998b].

Algebraic reconstruction techniques (ART) solve the problem in an iterative scheme. ART can differ in the way the corrective term is determined, but the iteration is always performed on a ray by ray basis until the calculated projection p_i^k of the iteration k is as close as possible to the measured data p_i^e [*Gilbert,* 1972]. All iterative algorithms start with a first estimate; its selection is of primary importance for the applicability of a method and for the number of iterations. Often, a homogeneous distribution is selected. For the atmospheric approach, if the underlying emission processes are well known, model distributions such as Chapman functions can be used instead. Since models about the F region dynamics are still very limited, we retrieve the initial estimate from the observed data.

Although algebraic and statistical methods are very competitive [*Frey et al.,* 1998b; *Nygrén et al.,* 1996; *Verhoeven,* 1993], we choose an algebraic technique. The flexibility provided by the ray by ray iteration allows the use of single scans as well as images. They are easily extendible to 3-D-approaches, and a priori information can be easily implemented. Our method was initially developed as multiplicative ART (MART) for stereographic auroral optical observations. It uses the multiplicative updating scheme combined with a back projection (BP). The BP projects each projection to the space by filling each line of sight with the data of the according projection and sums the projections [*Peyrin,* 1985]:

$$\hat{f}(x,y) = \frac{T}{T'} \cdot \sum_{i,\theta} b_{i\theta}^{xy}\, p_i(\theta), \quad (4)$$

with the density T of the element and the density T' of the complete array. This method is very fast, but the many simplifications generally return cell contents that are too high.

In the applied MART the initial estimate is reconstructed from the BP of the projections:

$$\hat{f}(x,y) = b_{i\theta}^{xy}\ p_i(\theta), \tag{5}$$

where each element is assigned the corresponding back projected data.

MART has successfully been used for the 3-D reconstruction of the volume emission in an auroral arc. The good correspondence between the reconstructed volume emission and the electron density measured by the European Incoherent Scatter (EISCAT) radar was later used to cross calibrate the volume emission and to estimate the ionospheric conductivity in a large area around the radar site [*Frey et al.*, 1998a].

Since the most important goal of tomography is the agreement between the reconstructed $\hat{f}(x,y)$ and the original distribution $f(x,y)$, a quantitative reconstruction parameter Λ_k is defined:

$$\sum_x \sum_y \sqrt{[f(x,y) - \hat{f}(x,y)]^2} = \Lambda_k \cdot \sum_x \sum_y f(x,y). \tag{6}$$

In any practical case, only the observations (line integrals) are known quantities. Therefore we also calculate the corresponding relation for the projections, and a λ_k is defined:

$$\sum_i \sum_\theta \sqrt{[p_i^k(\theta) - p_i^e(\theta)]^2} = \lambda_k \cdot \sum_i \sum_\theta p_i^e(\theta). \tag{7}$$

3. Limb Tomography Modeling

As the F region airglow tracks the density of excess ionization, it is dominated by horizontal or vertical plasma motions of the ionosphere rather than directly by gravity waves. Hence emission patterns are expected to be very diverse in size, intensity, and emission peak heights. Thermospheric emission rates were derived with WINDII on UARS, assuming horizontal homogeneity.

The WINDII data, shown in Plate 1, were taken with a view angle of 45° with respect to the satellite orbit track. Thus each observation is completely independent of the next one, making the data set unsuitable for tomographic analysis. Nevertheless, the data clearly show the structure of the instantaneous observations. The observed structures are representative of those we would measure on orbit with a similar imager pointing in the orbit plane. Hence a simulated data set with a similar distribution of the volume emission would allow a realistic test of the tomographic analysis.

Critical factors influencing reconstruction with real observations are noise reduction, geometry correction, and sensitivity calibration. In this simulation, we consider noise to be the most critical factor. To account for its influence on the quality of the reconstruction, two independent noise components were added to each projection:

$$p' = p + n_1 * \sqrt{p} + n_2, \tag{8}$$

where n_1 is proportional to the emission (photon noise) and n_2 is fixed (read out noise). This method gives an approximation of using an image intensifier and a CCD camera with certain read out noise. We use a typical signal-to-noise ratio (S/N) of 35 dB according to *Verhoeven* [1993], where

$$S/N = 10 \log \left(\sum_i p_i^2 / \sum_i \Delta p_i^2 \right) \tag{9}$$

and Δp_i is the error in each ray sum caused by the noise.

To reduce the influence of noise, we applied a median filter. Plate 2 (left) shows an ideal 2-D limb view, the noise deterioration, and the result of a median filtering. In this case, we used a field of view of 10° by 10° assuming homogeneity perpendicular to the orbit plane. The intensity profiles shown in Plate 2 (right) correspond to vertical cuts through the field of view in the orbit plane.

All tomographic techniques provide only an estimate of the original object function based on available projections. The accuracy and resolution vary among the various methods. Even the same method may perform differently for different objects or different methods of collecting the projections. Theoretical comparisons from one case to another are very difficult [*Gordon and Herman*, 1974]. This is especially true with respect to the object properties such as homogeneity, smoothness, symmetry, or steepness of intensity gradients.

To get an estimate of the resolution of horizontal and vertical parameters, we simulated emission features as height-dependent Chapman functions with a horizontal Gaussian distribution and arranged them periodically along the orbit track. Various scale heights control the thickness of the emission layer; the half width of the Gaussian distribution controls the horizontal wavelength. To monitor the resolution, we compared the structural information in limb projections, which is controlled by a horizontal wave parameter as well as a vertical parameter of the emission layer. The data in Figures 1a and 1b represent the limb scans from a thick layer and a thin layer, respectively, comprising the parameters from the WINDII data. Figures 1a and 1b compare limb scans obtained under the same geometry from an orbit at 600 km but with different horizontal wave parameters ranging from 250 to 1000 km. As the wavelength becomes shorter, we lose structural information in the limb projection and hence resolution of the tomographic result. For each horizontal parameter the limb scans from the thick layer in Figure 1a show less structure than the limb scans from the thin layer in Figure 1b. For comparison, Figure 1c shows limb

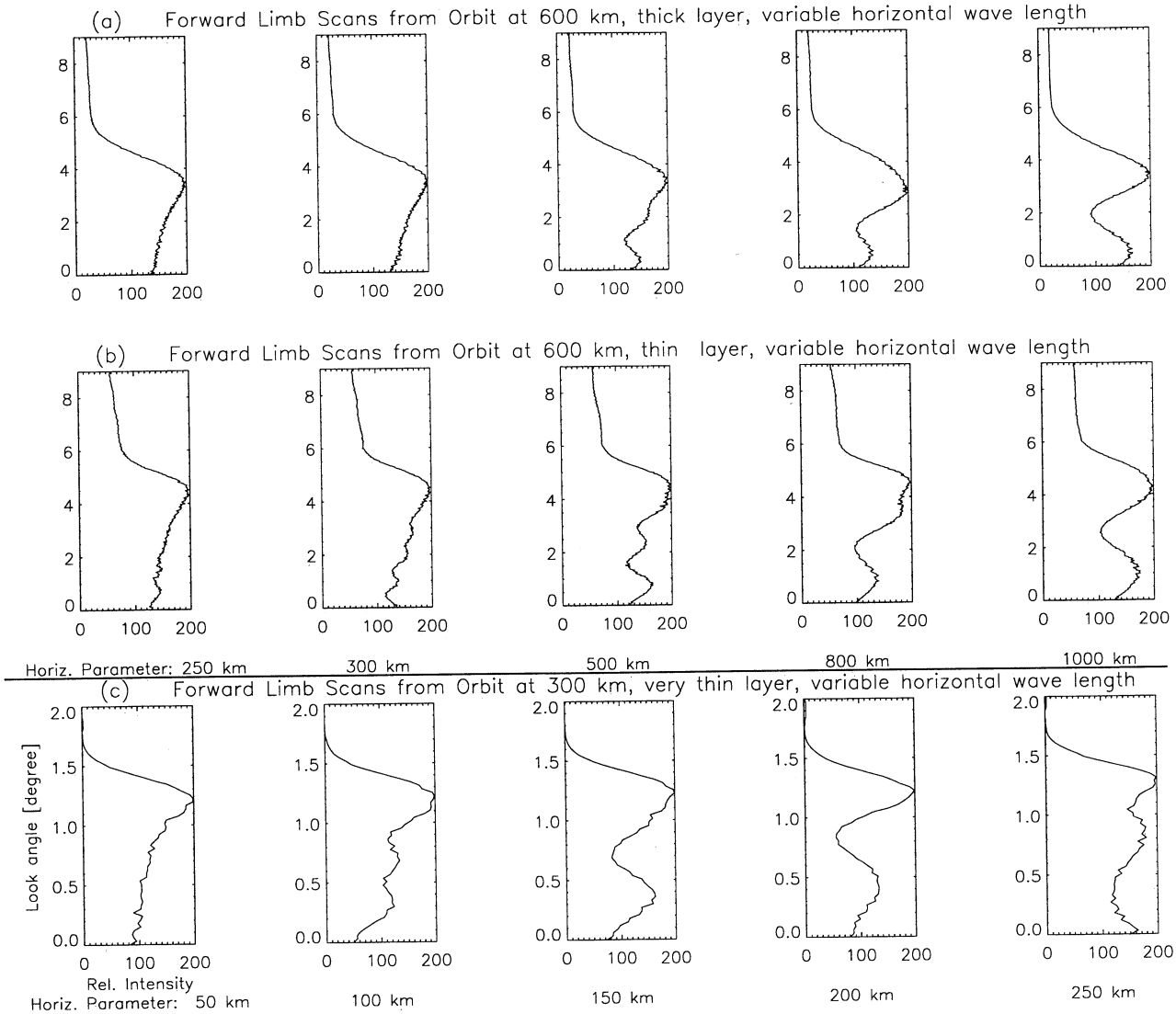

Figure 1. Forward limb scans compared for different original data. (a) and (b) Simulations of the observation of 630 nm emission from an orbit at 600 km altitude. The emission layer in Figure 1a is about 200 km thick with peak heights at 230 km. The layer in Figure 1b is about 90 km thick with peak heights at 260 km. (c) Simulations of the observations of the emission within a very thin layer (thickness 20 km) with peak heights at 90 km from an orbit at 300 km altitude. For all rows the horizontal parameters increase from left to right. For all columns the thickness decreases from top to bottom.

scans from emissions in the relatively thin layer around altitudes of 90 km obtained from an orbit at 300 km as investigated by *McDade and Llewellyn* [1993]. In Figure 1c the horizontal parameter resulting in feasible structures in limb scan is even smaller, ranging from 50 to 250 km.

Figures 1a-1c show a dependence on the ratio of the horizontal to the vertical parameter. Especially under the very limited viewing directions of limb projections, this ratio determines when the integrations along the lines of sight are sufficiently different. They are most different when the lines of sight match with symmetry axes of individual structures [*Verhoeven*, 1993]. Plates 3-5 show the different layers and one arbitrary limb scan and compare the horizontal and vertical profiles of the original and reconstructed data. They illustrate the sensitivity of the resolution of the tomographic result to both viewing direction and object property. The fluctuations of the amplitude shown in all examples result from the change in the angular coverage along the satellite track.

In Plate 3 we have the best coincidence between the original data (solid line) and the reconstructed data (dashed line) for the horizontal parameter. The fluctuations in the amplitude of the horizontal profile are significantly reduced compared to their counterparts in Plates 4 and 5. As indicated in the limb scan (Plate 3, middle left), lines of sight below 2.5° would hit the

Earth. Therefore the viewing direction is more downward directed and leads to deterioration in the quality of the vertical profile. This example of a quasi-limb view demonstrates good tomographic conditions to obtain both horizontal and vertical parameters. However, this constellation is not applicable for our investigation of the 630 nm emission because of albedo contamination. In Plate 4 the limb scan is less structured, but one can still determine the horizontal parameter. Regardless of the viewing direction, the vertical profile of the reconstructed data deteriorates as the original data lose horizontal homogeneity. In Plate 5 the reconstructed horizontal profile does not reveal any signature of the horizontal modulation in the original data as a result of the unstructured limb scan. It also has the strongest fluctuation in the amplitudes. The original data are more homogeneous horizontally. Therefore we find the best recovery of the vertical parameter. For our approach we determine this as the cutoff situation.

Parameters along symmetry axes that are closest to the viewing directions have the best resolution. Therefore both homogeneous and isolated structures can be well reconstructed. Apparently, the structures in Plate 4 are not isolated enough.

When a limited angular range does not allow such symmetry match, an increase in the number of projections within that range would not improve the result. Only additional downward observations reduce the error, as shown in Plate 3 while the sampling rates in Plates 3 and 4 are the same.

Under ill-posed conditions, as in satellite limb tomography, the purpose of the application determines the resolution. Since we are interested in both the horizontal and the vertical parameter, we put the cutoff of applicability at a horizontal wavelength of 300 km for the thicker layer and of 250 km for the thinner layer. For the very shallow layer in Figure 1c, structures are maintained even below 100 km. However, for the success in the reconstruction of wave-modulated emission patterns the orientation of the wave front is of great importance [*Nygrén et al.*, 1998]. Therefore these are only estimates of the range of wavelength possible to restore when the orientation of the wave front is tomographically favorable.

4. Simulated Limb Measurements From Ground-Based Data

In contrast to the airglow pattern in the mesopause region, we do not expect well-developed periodicity. As the WINDII data indicate, F region airglow patterns are extended single or compound structures of different intensity gradients and peak heights separated by depletion zones. To match that spatial inhomogeneity as realistically as possible, we used directly measured electron densities converted into volume emission rates as shown in Figure 2. These ionosonde data, from a campaign to observe 2-D signatures of gravity waves in the thermosphere/ionosphere system from Aerocibo, Puerto Rico, were used to relate ground-based observations of 630 nm with F region gravity waves [*Mendillo et al.*, 1997].

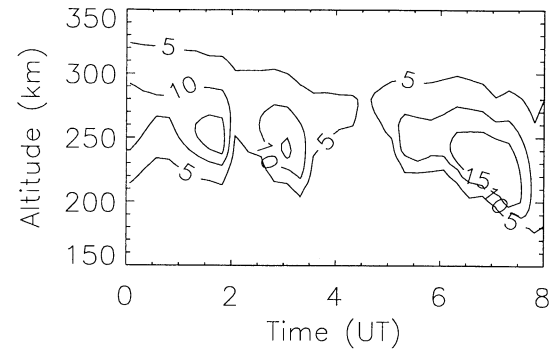

Figure 2. The airglow 630 nm emission, shown in an altitude versus time grid. The volume emission rate (photons $cm^{-3}s^{-1}$) was computed from electron density measurements by *Mendillo et al.* [1997].

For the conversion of emission rates from a height-time grid into an orbit plane we assumed the structures were moving at 200 ms^{-1}. The data were then concatenated to fill the orbit track of about 10,000 km at altitudes from 200 to 270 km altitude. This provides single structures with a horizontal length between a few hundred and a few thousand kilometers at peak heights around 240 km separated by regions of extinguished emissions.

A comparison with the WINDII data shows that this is a realistic model with structure sizes of the lower limits.

Plate 6 shows the irregular altitude dependence of the source distribution in the orbit plane at altitudes versus the orbit track. If the field of view is very small and/or the look direction is closer to the local horizon, the precision of the horizontal profiles is more affected than the precision of the vertical ones. This becomes an important constraint for satellite limb tomography of the 630 nm emission, where the intersection of lines of sight with near-Earth layers has to be avoided by a narrow field of view. Therefore we combine a small field of view of 9° with tangent heights between 60 and 400 km.

Satellite limb tomography differs from the traditional tomography where all projections intersect in one point and the object of interest is smaller than the field of view. Because of the motion of the satellite, any finite set of consecutive measurements results in an inhomogeneous angular coverage using all possible angles only at the center part. For a given field of view the larger the orbit segment, the larger the range with feasible tomographic conditions, assuming stationary processes during that overpass. Considering overpass periods of about 10 min, the stationary condition is not a con-

straint for wave periods over 1 hour. A horizontal traveling speed of 60 ms^{-1} in the orbit plane would lead to an uncertainty of about 40 km of a horizontal structure size if the time interval between the first and the last projection is about 10 min.

For this study, every 6 s, limb scans were taken along an orbit segment that centers the large structure in Plate 6 with the high intensity at lower altitudes and its faint predecessor at higher altitudes within the region of best angular coverage. Both features cover about 1800 km.

For one such overpass we have constructed a keogram, a collage of vertical limb scans extracted along the orbit segment, shown in Plate 7. The keogram already gives an impression about the irregularities, though horizontal and vertical information are still superimposed. Tomographically, these irregularities yield different geometric configurations, leading to different horizontal and vertical resolution during the overpass.

The goal is to invert a time series of 1-D limb scans in the orbit plane into the 2-D distribution of the volume emission in order to quantitatively analyze its modulation by electrodynamic forces in combination with gravity waves. The BP and its inverse are the key elements in the iterative algorithm described here. Because the total intensity within the images has to correspond to the integrated source distribution, some pixels at the outer surface of the object contain intensity that is missing in the center pixels. This is also most likely the reason why radio tomography tends to overestimate the electron density on the topside of the reconstruction [*Walker et al.*, 1996] and to produce thicker layers [*Nygrén et al.*, 1996].

Figure 3 shows the quality parameters for the volume emission and the brightness as expressed by (6) and (7) for an increasing number of iterations. Both parameters demonstrate best results after two iterations. The brightness parameter is more affected by the BP be-

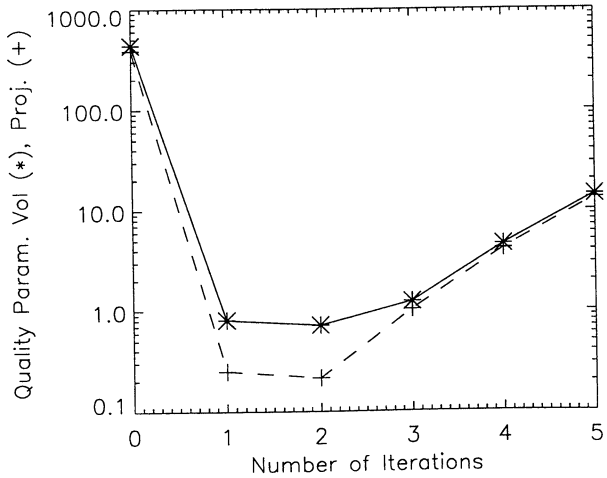

Figure 3. Quality parameter for the volume emission and the brightness for an increasing number of iterations. The zero iteration corresponds to the initial guess.

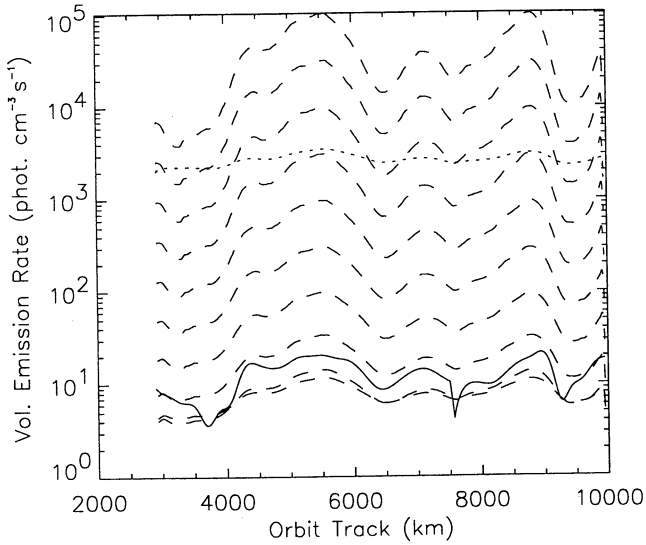

Figure 4. Comparison of horizontal profiles of the model at 250 km (solid), the initial guess made by back projection (dotted), and the reconstructed data after subsequent iterations (dashed). The different profiles correspond to different iterations.

cause of the additional use of its inverse for projection. The increase in the quality parameter after passing a minimum is a phenomenon related to the ART, which constructs the projections with random errors. Those errors increase with successive iterations as well as with more projections [*Gilbert*, 1972].

In Figures 4 and 5, the dotted lines show how the horizontal and vertical profiles of the initial estimate of volume emission are smoothed by the BP compared to the model data (solid lines). The dashed lines compare the

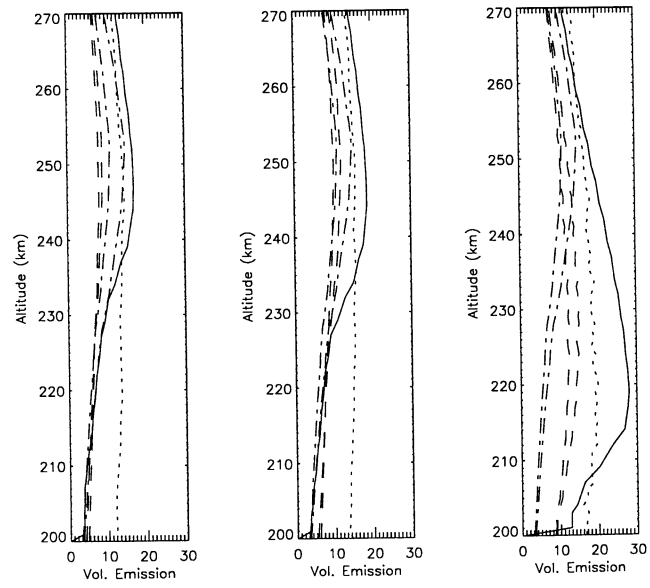

Figure 5. Comparison of the vertical profiles of volume emission rates (photons $cm^{-3}s^{-1}$) at (left) A, (middle) B, and (right) C, corresponding to the explanation in Figure 4. For a better visualization the data of the dotted and dash-dotted lines are scaled by constant factors.

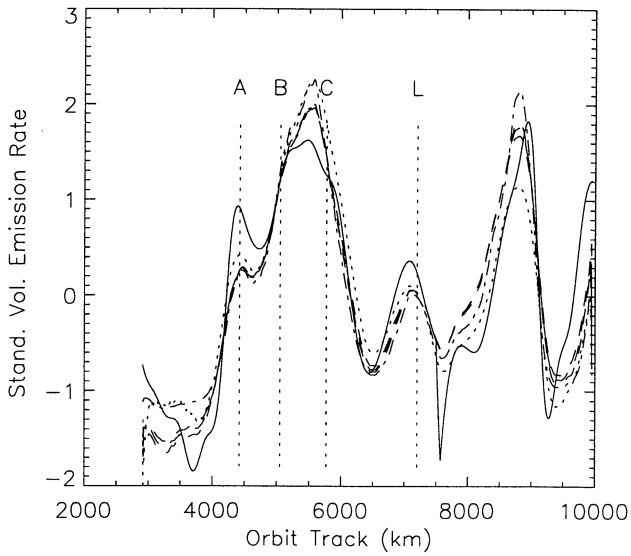

Figure 6. Horizontal profiles of the standardized volume emission rate (relative units) at 250 km: model (solid), initial guess (dotted), and first three iterations (dashed). Field of view is 9°.

results of the iterations. The intensity increases with the number of the iteration. The multiplicative correction in the first iteration corrects most of the washed out effect of the BP and reveals the shape of the distribution function. This explains the strong improvement of the quality parameter in Figure 3. The further increase in magnitude is due to the repetition of the BP and its inverse during the iterative processing. The horizontal profile after the second iteration fits the original data with a residual mean square (RMS) of 4.8 photons $(cm^3s)^{-1}$.

The multiplicative correction results in a size displacement of the profiles that is comparable to additive and proportional translation of data profiles. Such size displacement can often partially be removed by standardizing the data [*Romesburg,* 1984]. Standardizing is very common in multivariate analysis when different data have to be compared. The data are processed to have a mean of 0 and a variance of 1. If we apply standardization to our reconstructed data, we can reduce the separation of the profiles contributed by the BP.

Plate 8 demonstrates how standardizing the data renders the emission features. It shows the standardized model (Plate 8, top) and its standardized reconstruction (Plate 8, middle) in an orbit length versus altitude grid with the same color scale. The pixel resolution in the reconstructed plane is 10 km by 1 km. The unstandardized data after the second iteration are shown in Plate 8 (bottom) with a different color scale. The emission features are much more washed out.

While the limb observations themselves can qualitatively reveal the global pattern of higher intensities, as seen in Plate 7, all features of the very inhomogeneous data model are recovered very well in horizontal as well as in vertical direction. Figure 6 shows the standardized horizontal profile extracted at 250 km altitude through all structures. The horizontal parameters of the features between A and L can be determined with an error of 20%. For the large feature at the center, for instance, the uncertainty is about 180 km.

Plate 8 shows the inhomogeneous angular coverage due to the moving satellite, with the two features of most interest in the center. The dramatic increase in quality of the reconstructed data at the beginning corresponds to the slow increase in the number of intersecting lines of sight of the forward limb observations. For the same reason we observe the more gradual decrease in quality at the end of the orbit segment. Standardizing the data does not remove the amplitudinal fluctuations generated by the inhomogeneous angular coverage and the limited angular view.

Figure 7 shows how standardization improves the fit of the vertical profiles. The three vertical profiles cover the contrast of the faint feature and the maximum brightness next to it. In Plate 8 the position of the profiles are marked by solid lines and labeled for further reference. The relative constellation between the emission structure and the field of view of the limb instrument is unpredictable and varies along the orbit segment. Hence the vertical profiles differ in their agreement with the original data.

In the first profile, extracted in the faint feature A, the best shape similarity is given for heights up to the intensity peak, matching its position well. Above the maximum the profiles are more separated. The data in profiles A and B are best recovered where the two features do not interfere on the same line of sight. The second profile at B is extracted close to where the inter-

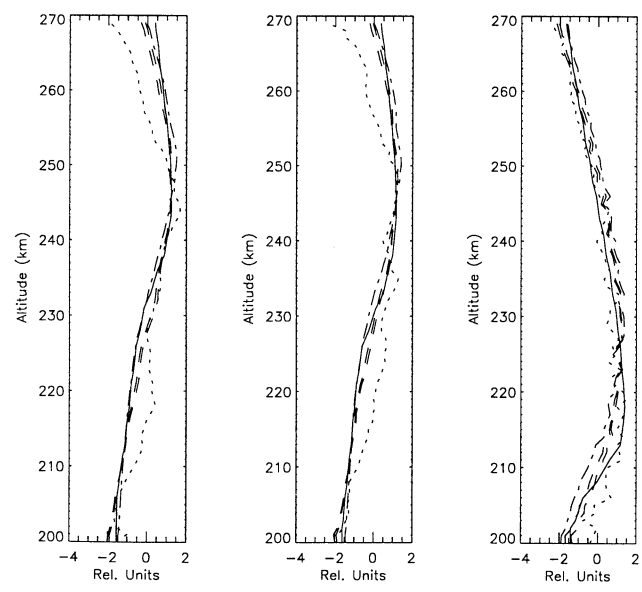

Figure 7. Vertical profiles of the standardized volume emission rate (relative units) at (left) A, (middle) B, and (right) C: model (solid), initial guess (dotted), and first three iterations (dashed). Field of view is 9°.

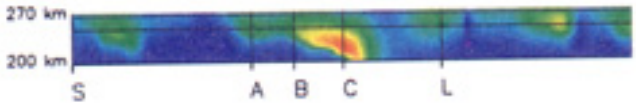

Plate 6. Altitude dependence of the source distribution (model) along the orbit track. S and L mark the orbit segment. Vertical profiles were extracted at the positions A, B, and C. The indicated heights correspond to the horizontal profiles.

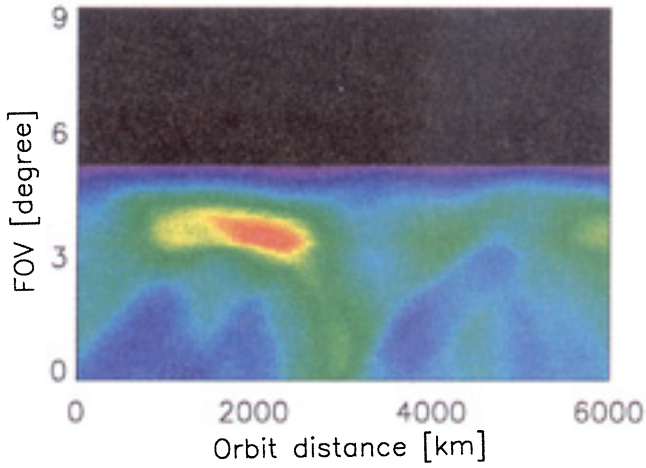

Plate 7. Collage of vertical limb scans, taken every 6 s along the orbit segment.

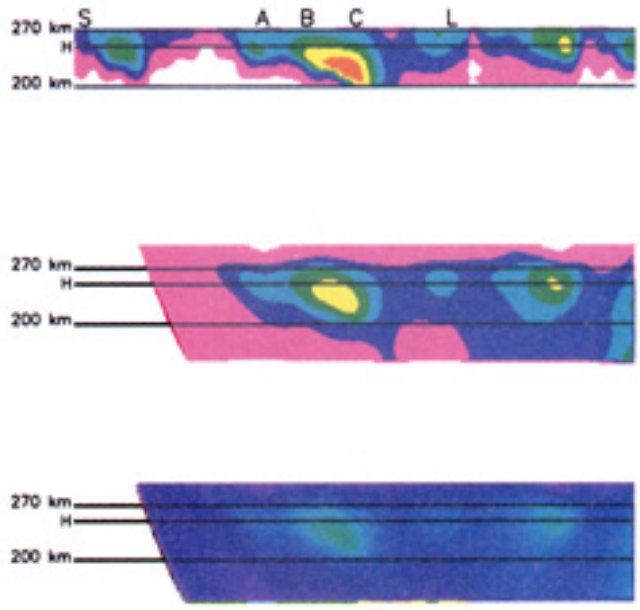

Plate 8. Comparison of shape similarity of (top) the model data after standardizing and the (middle) reconstructed data after three iterations. (bottom) The nonstandardized reconstructed data in a different color scale.

secting profiles indicate optimal viewing geometry after several iterations. The shape displacements between the profiles after the second iteration and the profile of the model is < 10 km. The intensity maximum of the reconstructed profile, also extracted at the large and bright structure, is shifted upward by about 10 km relative to the model data. The remaining shape difference is due to the relative geometry between the two features and the intersecting lines of sight rather than to the size displacement due to BP.

Standardizing the data helps to reproduce the shape of the profiles. To recover absolute magnitudes from the standardized data requires the knowledge of the mean and the standard deviation of the original distribution. Destandardizing the data will significantly improve the result even if the required information is deduced from the reconstructed data set. In Figures 8 and 9, we compare the original data (solid lines) with data of the second iteration destandardized with the mean and standard deviation of the original data (dashed lines) and with the average of the data sets after the second and third iteration (dotted lines). Using the mean and standard deviation of the original data improves the RMS of the horizontal profile from 4.8 to 2.1. Using the average of the second and third iterations yields in an RMS of 2.4. For the vertical profiles the RMS improves from 5.1 to 1.0 and 2.4, respectively, at A, from 4.4 to 0.9 and 2.14 at B, and from 8.7 to 1.9 and 2.2 at C. The results of the vertical profiles differ by a factor of 2. This reflects the fact that the resolution of the reconstructed data varies with the varying tomographic conditions during one overpass.

5. Conclusions

Results of tomographic inversions strongly depend on the quality of observational geometry, on the properties, and on a priori knowledge of the object. Those conditions determine the tomographic technique and how far it can be adjusted to the current situation. We presented a technique that is very flexible within a wide range of measurements, especially under the unpredictable geometry faced by space-born observations of the F region emission. To improve the results, the algorithm can instantly be adjusted to the object by preselecting the ranges of interests from the keogram. Using only the limb observations reduces the instrumentation complexity and permits the use of emission features in a wavelength range where the atmosphere is transparent. In wavelength regions where the atmosphere is opaque to the emission, additional nadir observations can easily be added. The computational effort can be controlled by the sampling rate and the pixel resolution in the reconstructed plane.

Under observational conditions that imply very strong constraints to the tomographic geometry we demonstrate reasonable results implementing only the nonnegativity constraint. Standardizing the reconstructed data is a guidance tool to determine the quality of the inversion condition and to extract the shape parameter.

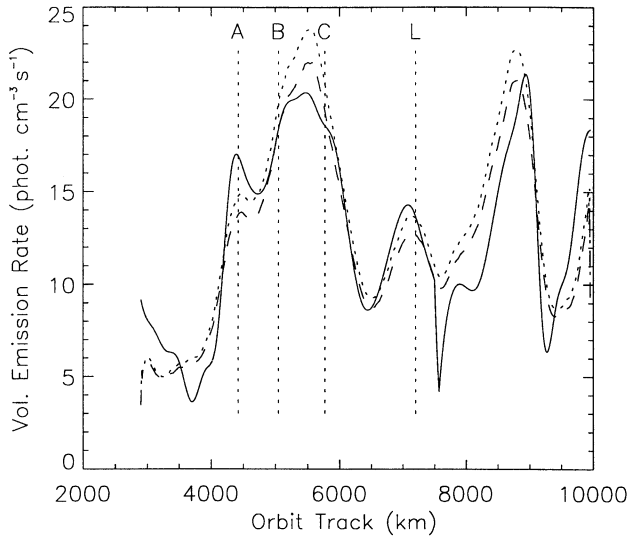

Figure 8. Horizontal profiles of volume emission rates at 250 km after destandardizing compared with the original data (solid). The reconstructed data fit the original data best when the mean and standard deviation of the original distribution is known (dashed). Usually, they have to be replaced by an estimate. The average of the reconstructed data from the two iterations with the best quality parameter provide estimates that yield in volume emission rates with an average error of 20% (dotted).

Within the range of homogeneous angular coverage and for horizontal parameters larger than the cutoff the absolute magnitude and the spatial information can be obtained with errors of 20% without any additional information or any assumptions of temperature or density distribution. Those data, if available, could even reduce the error by a factor of 2. Results based on the use of models are usually strongly dependent on the validity of the assumptions. This is especially critical in the case of the F region emissions because they are excited by ionic recombination, which is often modulated by the interaction of ionospheric electrodynamics and neutral winds. This requires the knowledge of atmospheric density rather than the easily accessible electron density in the emission region. This also limits the local and temporal validity of any photochemical and temperature model [*Meier and Picone,* 1994; *Fennelly et al.,* 1994]. In contrast, the thin emission layer at 90 km is generated by recombination processes where the trend is more uniform.

Reconstructed parameters, not biased by any assumptions, can be used to adjust the development of model functions and to help identify the actual trigger of large-scale modulation in the thermosphere. Though the technique is not yet an automated onboard routine, analysis in quasi-real time is possible for a large number of observations, as provided by global survey experiments.

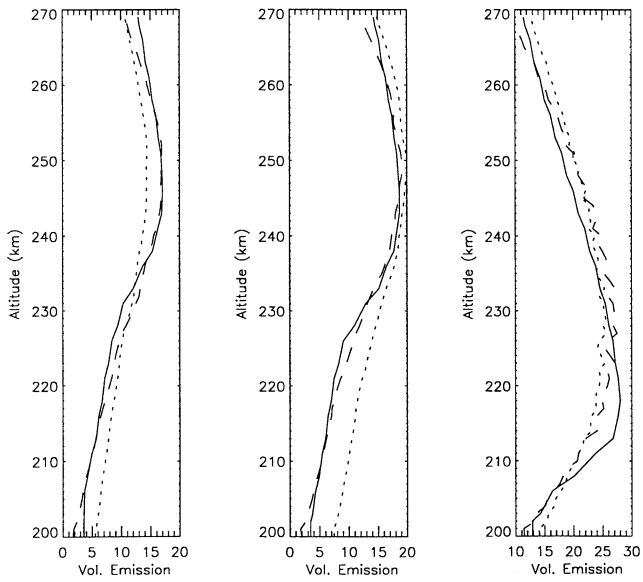

Figure 9. Vertical profiles of volume emission rates (photons cm^{-3}s^{-1}) at (left) A, (middle) B, and (right) C after destandardizing compared with the original data (solid) as explained in Figure 8.

Acknowledgments. We are very grateful to our colleagues G. Shepherd from York University, Toronto, Canada, and M. Mendillo from Boston University, Massachusetts, for providing the volume emission data.

H. Matsumoto thanks S. C. Solomon and another referee for their assistance in evaluating this paper.

References

Alexander, M. J., Interpretations of observed climatological patters in stratospheric gravity wave variance, *J. Geophys. Res., 103*, 8627–8640, 1998.

Allen, S. J., and R. A. Vincent, Gravity wave activity in the lower atmosphere: Seasonal and latitudinal variations, *J. Geophys. Res., 100*, 1327–1350, 1995.

Armstrong, E. B., The association of visible airglow features with a gravity wave, *J. Atmos. Terr. Phys., 44,* 325–336, 1982.

Aso, T., T. Hashimoto, M. Abe, T. Ono, and M. Ejiri, On the analysis of aurora stereo observations, *J. Geomagn. Geoelectr., 42,* 579–595, 1990.

Beach, T. L., M. C. Kelley, P. M. Kintner, and C. A. Miller, Total electron content variations due to nonclassical traveling ionospheric disturbances: Theory and Global Positioning System observations, *J. Geophys. Res., 102*, 7279–7292, 1997.

Bergman, J. W. and M. L. Salby, Equatorial wave activity derived from fluctuations in observed convection, *J. Atmos. Sci., 51*, 3791–3806, 1994.

Bernhardt, P. A.,et al., Two-dimensional mapping of the plasma density in the upper atmosphere with computerized ionospheric tomography (CIT), *Phys. Plasma, 5*, 2010–2021, 1998.

Budinger, T. F., and G. T. Gullberg, Three-dimensional reconstruction in nuclear medicine emission imaging, *IEEE Trans. Nucl. Sci., 21*, 2–20, 1974.

Burrage, M. D., M. F. Storz, C. C. Fesen, R. C. Robles, and V. J. Abreau, Solar tides in the equatorial upper thermosphere: A comparison between AE-E data and the TIGCM for solstice, solar minimum conditions, *J. Geophys. Res., 96*, 187–199, 1991.

Chamberlain, J. W., *Physics of the Aurora and Airglow*, edited by JJ. Chamberlain, reprint, 704 pp., AGU, Washington, D.C., 1995.

Coble, M., G. C. Papen, and C.S. Gardner, Computing two-dimensional unambiguous horizontal wave number spectra from OH airglow wave images, *IEEE Trans. Geosci. Remote Sens., 36*, 368–382, 1998.

Dewan, E. M., R. H. Picard, R. R. O'Neil, H. A. Gradier, J. Gibson, J. D. Mill, E. Richards, M. Kendra, and W. O. Gallery, MSX satellite observations of thunderstorm-generated gravity waves in midwave infrared images of the upper stratosphere, *Geophys. Res. Lett., 25*, 939–942, 1998.

Doe, R. A., J. D. Kelly, J. L. Semeter, and D. P. Steele, Tomographic reconstruction of 630.0 nm emission structure for a polar cap arc, *Geophys. Res. Lett., 24,* 1119-1122, 1997.

Fennelly, J. A., D. G. Torr, P. G. Richards, and M. R. Torr, Simultaneous retrieval of the solar EUV flux and neutral thermospheric O, O_2, N_2, and temperature from twilight, *J. Geophys. Res., 99*, 6483-6490, 1994.

Fesen, C. G., and V. J. Abreu, Modeling the 6300-Å low latitude nightglow, *J. Geophys. Res., 92*, 1231–1239, 1987.

Fesen, C. G., and P. B. Hays, Two-dimensional inversion technique for satellite airglow data, *Appl. Opt., 21,* 3784–3791, 1982.

Frederick, J. E., Influence of gravity wave activity on lower thermospheric photochemistry and composition, *Planet. Space Sci., 27*, 1469–1477, 1979.

Frey, H. U., S. Frey, B. S. Lanchester, and M. Kosch, Optical tomography of the aurora and EISCAT, *Ann. Geophys., 16*, 1332–1342, 1998a.

Frey, H. U., S. Frey, D. Larson, T. Nygrén, and J. Semeter, Tomographic methods for magnetospheric applications, in *Science Closure and Enabling Technologies for Constellation Class Missions*, edited by V. Angelopoulos and P. Panetta, pp. 72–77, University of California, Berkeley, California 1998b.

Frey, H. U., S. B. Mende, J. F. Arens, P. R. McCullough, and G. R. Swenson, Atmospheric gravity wave signatures in the infrared hydroxyl OH airglow, *Geophys. Res. Lett., 27*, 41-44, 2000.

Frey, S., H. U. Frey, D. J. Carr, O. H. Bauer, and G. Haerendel, Auroral emission profiles extracted from three-dimensionally reconstructed arcs, *J. Geophys. Res., 101,* 21,731–21,741, 1996.

Fritts, D. C., and Z. Luo, Gravity wave excitation by geostrophic adjustment of the jet stream, part I, Two-dimensional forcing, *J. Atmos. Sci., 49*, 681-697, 1992.

Fritts, D. C., and R. A. Vincent, Mesospheric momentum flux studies at Adelaide, Australia: Observations and a gravity wave-tidal interaction model, *J. Atmos. Sci., 44*, 605–619, 1987.

Garcia, F. J., M. J. Taylor, and M. C. Kelley, Two-dimensional spectral analysis of mesospheric airglow image data, *Appl. Opt., 36,* 7374–7385, 1997.

Gardner, C. S., and M. J. Taylor, Observational limits for lidar, radar, and airglow imager measurements of gravity wave parameters, *J. Geophys. Res., 103*, 6427–6437, 1998.

Gilbert, P., Iterative methods for the three-dimensional reconstruction of an object from projections, *J. Theor. Biol., 36,* 105–117, 1972.

Gordon, R., and G.T . Herman, Three-dimensional reconstruction from projections: A review of algorithms, *Int. Rev. Cytol., 38*, 111-151, 1974.

Gustavsson, B., Tomographic inversion for ALIS noise and resolution, *J. Geophys. Res., 103,* 26,621–26,632, 1998.

Hayner, D. A., and W. K. Jenkins, The missing cone problem in computer tomography, in *Advances in Computer Vision and Image Processing,* JAI, Greenwich, Conn. 1984.

Hines, C. O., On the nature of traveling ionospheric disturbances launched by low-altitude nuclear explosions, *J. Geophys. Res., 72*, 1877–1885, 1967.

Hirota, I., Climatology of gravity waves in the middle atmosphere, *J. Atmos. Terr. Phys., 46*, 767–773, 1984.

Kamalabadi, F., W. C. Karl, J. Semeter, D. M. Cotton, T. A. Cook, and S. Chakrabarti, A statistical framework for space-based EUV ionospheric tomography, *Radio Sci., 34*, 437-477, 1999.

Luo, Z., D. C. Fritts, R. W. Portmann, and G. E. Thomas, Dynamical and radiative forcing of the summer mesopause circulation and thermal structure, 2, Seasonal variations, *J. Geophys. Res., 100*, 3129-3137, 1995.

McDade, I. C., and E.J. Llewellyn, Satellite airglow limb tomography: Methods for recovering structured emission rates in the mesospheric airglow layer, *Can. J. Phys., 71*, 552–563, 1993.

McIntyre, M. E., On dynamics and transport near the polar mesopause in summer, *J. Geophys. Res., 94*, 14,617–14,628, 1989.

Meier, R. R., and J. M. Picone, Retrieval of absolute thermospheric concentrations from the far UV dayglow: An application of discrete inverse theory, *J. Geophys. Res., 99*, 6307-6320, 1994.

Mende, S. B., H. U. Frey, S. P. Geller and G. R. Swenson, Gravity wave modulated airglow observations from spacecraft, *Geophys. Res. Lett., 25*, 757–760, 1998.

Mendillo, M., J. Baumgardner, D. Nottingham, J. Aarons, B. Reinisch, J. Scali, and M. Kelley, Investigations of thermospheric dynamics with 6300-Å images from Arecibo observatory, *J. Geophys. Res., 102*, 7331–7343, 1997.

Miller, C. A., W. E. Swartz, M. C. Kelley, M. Mendillo, D. Nottingham, J. Scali, and B. Reinisch, Electrodynamics of midlatitude spread F, 1, Observations of unstable gravity wave-induced ionospheric electric fields at tropical latitudes,*J. Geophys. Res., 102*, 11,533-11,538, 1997.

Natterer, F., *The Mathematics of Computerized Tomography*, John Wiley, New York, 1986.

Nygrén, T., M. Markkanen, M. Lehtinen, D. Tereshchenko, B. Z. Khudukon, O. V. Evstafiev, and P. Pollari, Comparison of F-region electron density observations by satellite radio tomography and incoherent scatter methods, *Ann. Geophys., 14,* 1422–1428, 1996.

Nygrén, T., M.J. Taylor, M. Lehtinen, and M. Markkanen, Application of tomographic inversion in studying airglow in the mesopause region, *Ann. Geophys., 16,* 1180–1189, 1998.

Peyrin, F. C., The generalized back projection theorem for cone beam reconstruction, *IEEE Trans. Nucl. Sci., 32*, 1512–1519, 1985.

Raymund, T. D., S. E. Pryse, L. Kersley, and J. A. T. Heaton, Tomographic reconstruction of ionospheric electron density with European incoherent scatter radar verification, *Radio Sci., 28,* 811–817, 1993.

Romesburg, H.C., *Cluster Analysis for Researchers*, Lifetime Learning, Belmont, California, 1984.

Semeter J., M. Mendillo, and J. Baumgardner, Multispectral tomographic imaging of the midlatitude aurora, *J. Geophys. Res., 104*, 24,565–24,585, 1999.

Shepherd, G.G., et al. WINDII, the wind imaging interferometer on the Upper Atmosphere Research Satellite, *J. Geophys. Res., 98*, 10,725-10,750, 1993.

Singh, S., F. S. Johnson, and R. A. Power, Gravity wave seeding of equatorial plasma bubbles, *J. Geophys. Res., 102*, 7399–7410, 1997.

Solomon, S. C., P. B. Hays, and V. J. Abreu, Tomographic inversion of satellite photometry, *Appl. Opt., 23,* 3409–3414, 1984.

Solomon, S. C., P. B. Hays, and V. J. Abreu, Tomographic inversion of satellite photometry, part 2, *Appl. Opt., 24,* 4134–4140, 1985.

Solomon, S. C., P. B. Hays, and V. J. Abreu, Auroral 6300 Å Emission: Observations and modeling, *J. Geophys. Res., 93,* 9867–9882, 1988.

Swenson, G. R., and C. S. Gardner, Analytical models for the responses of mesospheric OH and Na layers to atmospheric gravity waves, *J. Geophys. Res., 103,* 6271–6294, 1998.

Swenson, G. R., and A. Z. Liu, A model for calculating acoustic gravity wave energy and momentum flux in the mesosphere from OH airglow, *Geophys. Res. Lett., 25,* 477-480, 1998.

Swenson, G. R., M. J. Alexander, and R. Haque, Dispersion imposed limits on atmospheric gravity waves in the mesosphere: Observations from OH airglow, *Geophys. Res. Lett., 27,* 875-878, 2000.

Tarasick, D. W., and G. G. Shepherd, Effects of gravity waves on complex airglow chemistries, *J. Geophys. Res., 97,* 3185–3208, 1992.

Taylor, M. J., A review of advances in imaging techniques for measuring short period gravity waves in the mesosphere and lower thermosphere, *Adv. Space Res., 19,* (no. 4), 667-676, 1997.

Taylor, M. J., W. R. Pendleton Jr., S. Clark, H. Takahashi, D. Gobbi, and R. A. Goldberg, Image measurements of short-period gravity waves at equatorial latitudes, *J. Geophys. Res., 102,* 26,283–26,299, 1997.

Thomas, R. J. and T. M. Donahue, Analysis of Ogo 6 observations of the OI 5577 - A tropical nightglow, *J. Geophys. Res., 77,* 3557–3565, 1972.

Vallance Jones, A., et al., The ARIES auroral modeling campaign: Characterization and modeling of an evening auroral arc observed from a rocket and a ground-based line of meridian scanners, *Planet. Space Sci., 39,* 1677–1705, 1991.

Verhoeven, D., Limited-data computed tomography algorithms for the physical sciences, *Appl. Opt., 32,* 3736–3754, 1993.

Walker, I. K., J. A. T. Heaton, L. Kersley, C. N. Mitchell, S. E. Pryse and M. J. Williams, EISCAT verification in the development of ionospheric tomography, *Ann. Geophys. 14,* 1413-1436, 1996.

H. U. Frey, S. Frey, S. B. Mende, Space Sciences Laboratory, University of California, Berkeley, CA 94720-7450, USA (e-mail: sfrey@ssl.berkeley.edu)

(Received June 20, 2000; revised February 5, 2001; accepted February 5, 2001.)